ACS APPLIED MATERIALS & INTERFACES

www.acsami.org

Research Article

ORAOV 1 Detection Made with Metal Organic Frameworks Based on $Ti_3C_2T_x$ MXene

Yu-Ping Wei, Jing-Shuai Chen, Xing-Pei Liu,* Chang-Jie Mao,* and Bao-Kang Jin

Cite This: *ACS Appl. Mater. Interfaces* 2022, 14, 23726−23733

Read Online

ACCESS | Metrics & More | Article Recommendations | Supporting Information

ABSTRACT: In this work, a two-dimensional (2D) MOF sheet with electrochemiluminescence (ECL) activity is prepared with $Ti_3C_2T_x$ MXene as the metal precursor and the meso-tetra(4-carboxyl-phenyl) porphyrin (H_2TCPP) as the organic ligand. The atomically thin 2D $Ti_3C_2T_x$ MXene is utilized as the metal precursor and soft template to produce the MOF with a 2D nanosheet morphology ($Ti_3C_2T_x$-PMOF). $Ti_3C_2T_x$ MXene is a kind of strong electron acceptor, which can deprotonate H_2TCPP due to the high electronegativity and low work function of its terminal atoms. The deprotonated H_2TCPP continues to bind with Ti atoms to form the 2D MOF sheet. The ECL activity is inherited from H_2TCPP and stabilized by introducing Ag NPs. Then, we construct an ECL biosensor based on the Ag NPs/$Ti_3C_2T_x$-PMOF to detect the oral cancer overexpressed 1 (ORAOV 1). A bipedal three-dimensional DNA walker strategy is adopted to further improve the biosensor sensitivity. As expected, the biosensor exhibits sterling sensitivity and selectivity. The ECL biosensor responds linearly to ORAOV 1 concentrations in the range of 10 fM−1 nM, and the detection limit is as low as 3.3 fM (S/N = 3). It means that Ag NPs/$Ti_3C_2T_x$-PMOF is a potential material to design and construct the high-performance ECL biosensors.

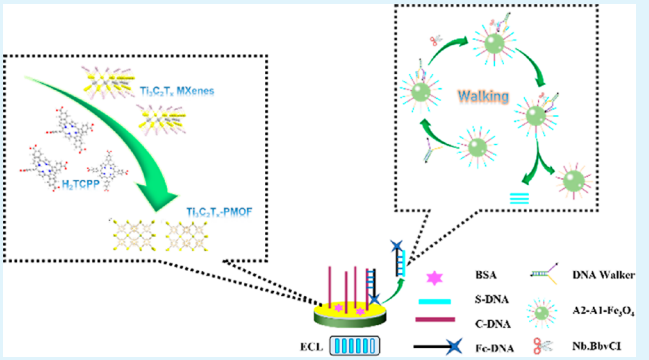

KEYWORDS: *$Ti_3C_2T_x$ MXene, $Ti_3C_2T_x$-PMOF, ORAOV 1, bipedal three-dimensional DNA walker*

$Ti_3C_2T_x$ MXene, an emerging two-dimensional (2D) material, which is produced by a wet hydrofluoric chemical treatment of Ti_3AlC_2 phases, has been widely used in catalysis, electrochemical supercapacitors, and biosensors owing to its excellent properties such as electrical conductivities, large surfaces, and biocompatibility.[1−5] After being etched by HF, the surface of $Ti_3C_2T_x$ MXene is terminated by −O, −OH, and −F.[6] These terminal groups with high electronegativity and low work function make the $Ti_3C_2T_x$ MXene a strong electron acceptor. In addition, the sufficient accessible surface of the 2D $Ti_3C_2T_x$ MXene makes them more vulnerable to attack by protonated organic ligands.[7] Due to large fluidity and good stability of electrons in the ring, porphyrin compounds have excellent luminescence electrochemical and photoelectric properties.[8,9] In recent years, there have been some reports on the improvement of porphyrin electrochemiluminescence (ECL) intensity by aggregating porphyrin compounds to form a MOF structure.[8,10,11] H_2TCPP contains a large planar aromatic ring and protons of carboxylic groups, which could attack and bind the surface atoms of $Ti_3C_2T_x$ MXene.[7] However, the formation of MOFs using $Ti_3C_2T_x$ MXene as the metal precursor and porphyrin as the organic ligand and their ECL property have not been reported. Hence, we try to synthesize a $Ti_3C_2T_x$-PMOF nanomaterial. Ag NPs are a wonderful nanomaterial because of their good electrical conductivity, high catalytic activity, and are easy to synthesize.[12] There have been some reports about synthesis of Ag@$Ti_3C_2T_x$ for lithium storage[13] or for constructing an electrochemical biosensor.[12] Ag NPs have been widely used in the ECL biosensor as a co-reactant promoter.[14,15] In this study, we build a ECL biosensor based on Ag NPs/$Ti_3C_2T_x$-PMOF.

Oral cancer overexpressed 1 (ORAOV 1) is a kind of candidate proto-oncogene located at chromosome band 11q13. Recent reports have shown that ORAOV 1 is the main driver of 11q13 gene amplification and has an important role in the carcinogenesis of a variety of human squamous cell carcinoma.[16,17] Moreover, Jiang et al. found that ORAOV 1 also participates in regulating the growth of cervical cancer cells.[16] Because of the low expression of ORAOV 1 and the complex composition of saliva, it is necessary to construct a high-performance biosensor for ORAOV 1 detection. DNA walker is a programmable and structurally controllable molecular machine based on precise complementary base

Received: January 10, 2022
Accepted: April 29, 2022
Published: May 10, 2022

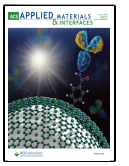

Scheme 1. Complete Fabrication Process for the ECL Biosensor

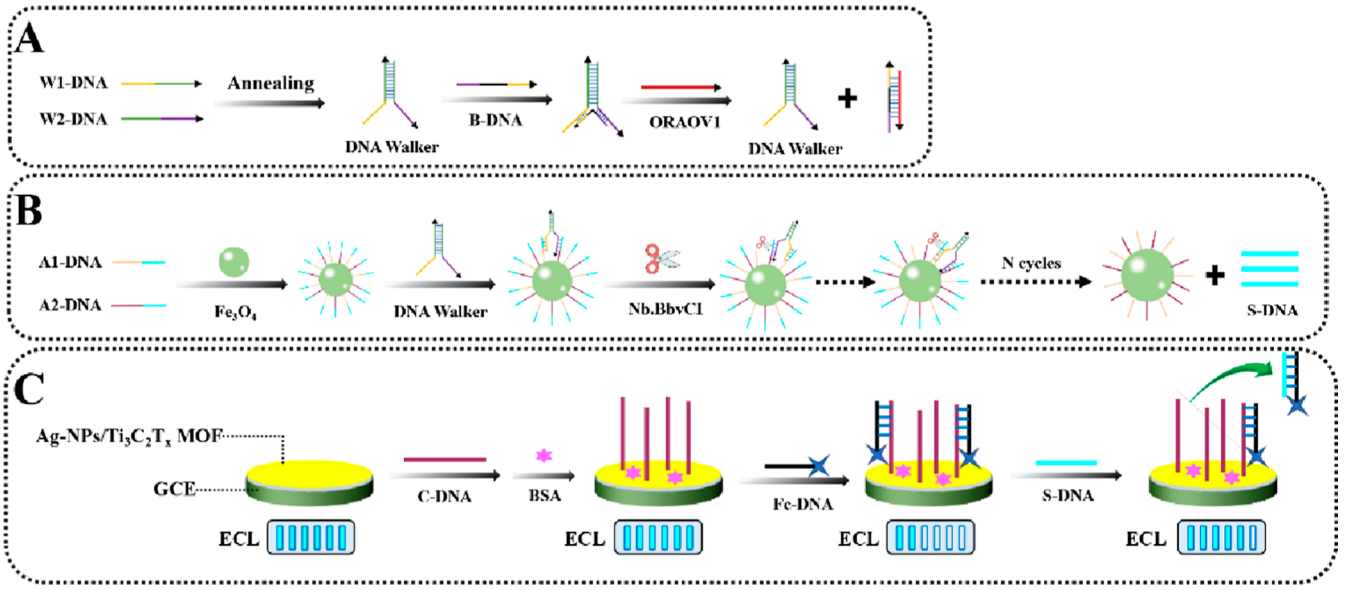

pairing of deoxyribonucleic acid.[17] Driven by chemical energy of biasing Brownian motion, the DNA walker can move along the predesigned tracks automatically.[18] The signal amplification strategy based on the DNA walker has been applied in the trace detection of oligonucleotides or microRNA.[19−21] For example, Li et al. combined the DNA walker-amplified strategy and DNA hydrogel-amplified signal probes for fluorescence detection of microRNA. The fluorescence biosensor exhibited a low detection limit of 1.1×10^{-4} fM.[22] Zhu Minghui et al. built an ultrasensitive photoelectrochemical sensor for TB detection, which relies on signal change triggered by a bipedal DNA walker.[23]

Based on the Ag NPs/$Ti_3C_2T_x$-PMOF and bipedal three-dimensional (3D) DNA walker, we built a highly sensitive and selective biosensor to detect the ORAOV 1. The sufficient accessible surface of delaminated 2D $Ti_3C_2T_x$ provides reaction sites for the protonated H_2TCPP and then forms a 2D MOF structure. The morphology and size of $Ti_3C_2T_x$-PMOF was measured by scanning electron microscopy and transmission electron microscopy. After being loaded with Ag NPs, the ECL intensity and stability had been improved significantly. Then, a 3D DNA walker was designed: a pair of longer chains which can be partially complementary are used as walking sequences. A shorter DNA (B-DNA) includes target recognition motif as the blocking strand. Fe_3O_4 magnetic nanospheres modified with track ligands served as the foothold. After the ORAOV 1 hybridized with B-DNA, the DNA walker was released and fueled by nicking endonuclease (Nb.BbvCI) to walk along the tracks. The detailed process is shown in Scheme 1.

EXPERIMENTAL SECTION

The chemical, materials, and apparatus are provided in the Supporting Information.

Preparation of Delaminated $Ti_3C_2T_x$ MXene. The delaminated $Ti_3C_2T_x$ MXene was prepared according to the previous reports with slight modification: Under stirring conditions, 1 g of Ti_3AlC_2 was slowly added to 40% HF solution in batches.[24] Also, the reaction system was stirred at 40 °C for 72 h. After adequate etching, the multilayered $Ti_3C_2T_x$ was washed with ultrapure water. The washing process was repeated until the supernatant is neutral. After that, the multilayered $Ti_3C_2T_x$ was collected by centrifugation. For delamination, the multilayered $Ti_3C_2T_x$ was redistributed in 10% TMAOH solution and stirred at room temperature for 12 h. In order to eliminate the extra TMAOH, the reaction product was centrifugated and washed with ultrapure water. The washing step was repeated until the pH of the supernatant is neutral. Then, the precipitate was obtained by centrifugation (12 000 r.p.m). The black powder sample was collected after vacuum-drying at 40 °C.

Preparation of $Ti_3C_2T_x$-PMOF Nanosheets and Ag NPs/$Ti_3C_2T_x$-PMOF Nanocomposites. 15 mg of the delaminated $Ti_3C_2T_x$ MXene was distributed in 10 mL of DMF and sonicated at an ice-water bath for 30 min. Then, 60 mg of tetrakis (4-carboxyphenyl) porphyrin was immersed in the solution and sonicated for 10 min. After that, the mixture was transferred to a Teflon autoclave and proceeded the solvothermal reaction was under 150 °C for 8 h. Finally, the precipitate was collected by centrifugation (12 000 r.p.m). In order to remove DMF, the precipitate was redistributed in methanol and stirred for 24 h. In this procedure, the color of methanol solution was purple. Then, the $Ti_3C_2T_x$-PMOF nanosheets were collected by centrifugation. The powder sample was dried under vacuum at 40 °C.

The as-synthesized $Ti_3C_2T_x$-PMOF nanosheets and 176 mg of $AgNO_3$ were distributed in 3 mL of ultrapure water. The mixed solution was stirred overnight in the darkness at room temperature to absorb enough Ag^+ on the nanosheet surface. Ag^+ was reduced by 20 mg of $NaBH_4$. Then, the Ag NPs/$Ti_3C_2T_x$-PMOF was obtained by centrifugation and washed with ultrapure water. Finally, the nanocomposite was distributed by ultrapure water and stored in the dark for use.

Assembly of Track Strands on Fe_3O_4 Surface. Fe_3O_4 was synthesized according to the report.[25] In order to link with A1 and A2, the carboxyl groups of Fe_3O_4 were activated by EDC and NHS. Briefly, 0.0087 g of NHS and 0.0062 g of EDC were added to 0.5 mg/mL of Fe_3O_4 solution (10 mM PBS buffer) and incubated at 37 °C for 1 h. After that, 7.5 μL of A1, 7.5 μL of A2, and 90 μL of activated Fe_3O_4 were blended and incubated at 37 °C for 2 h. Then, the mixture was magnetically separated. The precipitate was further incubated by 2% BSA to avoid the nonspecific adsorption. Finally, A2-A1-Fe_3O_4 was obtained after magnetic separation and redispersed in TE buffer. Also, the product was stored at 4 °C for usage.

Preparation of 3D DNA Walker. The mixture of 5 μL of W1 (5 μM) and 5 μL of W2 (5 μM) was heated at 95 °C for 10 min and slowly cooled down to 25 °C to form the DNA walker. Then, 5 μL of B (5 μM) was injected into the mixture and incubated at 37 °C for 2 h to block the walker. 20 μL of A2-A1-Fe_3O_4, 10 μL of Nb.BbvCI (10

https://doi.org/10.1021/acsami.2c00497
ACS Appl. Mater. Interfaces 2022, 14, 23726−23733

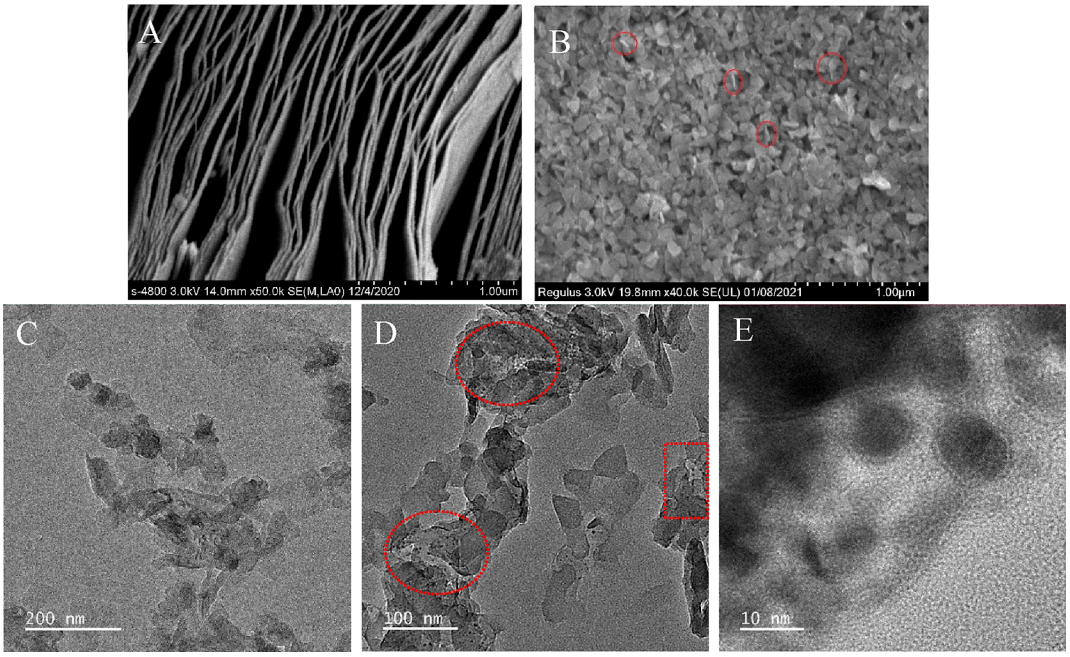

Figure 1. SEM images of multilayered Ti3C2T$_x$ MXene (A) and Ti3C2T$_x$-PMOF (B), TEM image of Ti3C2T$_x$-PMOF (C) and Ag NPs/Ti3C2T$_x$-PMOF (D), and HRTEM of Ag NPs/Ti3C2T$_x$-PMOF (E).

U/mL), 5 μL of different concentrations of ORAOV 1, and the blocked DNA walker solution were mixed and incubated at 37 °C for 2 h. After the DNA walker amplification reaction, the resultant reaction solution containing S-DNA was obtained by magnetic separation and stored in a fridge for usage.

Fabrication of the Biosensor and the Measurement Procedure. First, the glassy carbon electrode was polished by 0.3 μm alumina powder and then sonicated with ultrapure water and ethanol in turn to obtain a clean electrode surface. Then, 10 μL of Ag NPs/$Ti_3C_2T_x$-PMOF was deposited on the cleaned glassy carbon electrode (GCE) and dried in air. In order to be modified with C-DNA, 10 μL of terminal modified with the amine group C-DNA (6 μM) was added to the GCE, and then, the GCE was stored at 4 °C for 12 h. The C-DNA was anchored on the GCE by the Ag−N bond. Subsequently, to restrain nonspecific bindings, 10 μL of BSA (2%) was dropped on the resultant GCE and incubated at 37 °C for 30 min. Then, 10 μL of Fc-DNA (12 μM) was modified on the GCE through the specific binding with C-DNA. 10 μL of the resultant reaction solution containing S-DNA was deposited on the modified GCE. The GCE was incubated at 37 °C for 2 h to remove the Fc-DNA, and then, the ECL response signal of the modified GCE was restored. The modified GCE in each of the abovementioned steps has been thoroughly rinsed with TE buffer and dried by N_2. For ECL detection, the final GCE was measured in 0.1 M PBS buffer containing 0.1 M $K_2S_2O_8$, and the scanning potential ranged from 0 to −1.7 V, with a scan rate of 100 mV/s.

RESULTS AND DISCUSSION

Operating Principle of the 3D Walker. As shown in Scheme 1, first, a bipedal 3D walking strand was composed of two walking strands, which were named W1 and W2, respectively. The walking strands contain different sequences and can be partially complementary. After W1 hybridized with W2, the bipedal 3D walking strand was blocked by B-DNA. B-DNA was a small oligonucleotide containing the recognition motif of W1, W2, and the target. In the presence of ORAOV 1, the B-DNA was hybridized with ORAOV 1 and then released the DNA walker. Then, we designed 3D tracks. The amine-modified A1-DNA and A2-DNA were modified on the Fe_3O_4 nanoparticle to form DNA tracks. The released DNA walker strands (W1 and W2) were specifically recognized by track strands (A1and A2) at the start of the walking process. Fueled by nicking endonuclease (Nb.BbvCI), the DNA walker was moved along the tracks through shearing the foothold of tracks. Each step of the Nb.BbvCI nicking will generate the intermediate DNA (S-DNA). Due to the multiple-step walking, a large number of S-DNA were released and the concentration of ORAOV 1 was amplified. After magnetic separation, the S-DNA in the supernatant was dropped on the Fc-DNA/BSA/C-DNA/Ag NPs/$Ti_3C_2T_x$-PMOF/GCE to recognize and pair with the Fc-DNA, and then, the ECL response of Ag NPs/$Ti_3C_2T_x$-PMOF was restored. The degree of recovery was positively correlated with the amount of ORAOV 1.

Characterization of $Ti_3C_2T_x$ MXene, $Ti_3C_2T_x$-PMOF Nanosheets, and Ag NPs/$Ti_3C_2T_x$-PMOF Nanocomposite. The topography of multilayered $Ti_3C_2T_x$ is presented in Figure 1A. From Figure 1A, a typical accordion-like nanostructure of multilayered $Ti_3C_2T_x$ was observed. It proved that the Al layers were successfully etched out of the MAX phase (Ti_3AlC_2) through high concentration of HF. After the TMAOH intercalation and delamination, the $Ti_3C_2T_x$ MXene was synthesized. The X-ray diffraction (XRD) characteristic peak (Figure S1), which located at 5.94°, demonstrated the larger layer spacing of $Ti_3C_2T_x$ MXene. Then, the delaminated $Ti_3C_2T_x$ MXene and H_2TCPP were converted into $Ti_3C_2T_x$-PMOF. The scanning electron microscopy (SEM) images of $Ti_3C_2T_x$-PMOF are shown in Figure 1B. Different from $Ti_3C_2T_x$ MXene, the $Ti_3C_2T_x$-PMOF displayed a 2D sheet-like morphology with a relatively uniform size (around 100 nm). The transmission electron microscopy (TEM) images (Figure 1C) also proved the uniform size. The XRD pattern of $Ti_3C_2T_x$-PMOF (Figure 2A) was consistent with a previous report.[7] It was further confirmed that it was feasible to use $Ti_3C_2T_x$ MXene as a metal precursor and H_2TCPP as a ligand to synthesize MOFs. As for Ag NPs/$Ti_3C_2T_x$-PMOF, the TEM images (Figure 1D) show the existence of Ag NPs. The small

https://doi.org/10.1021/acsami.2c00497
ACS Appl. Mater. Interfaces 2022, 14, 23726−23733

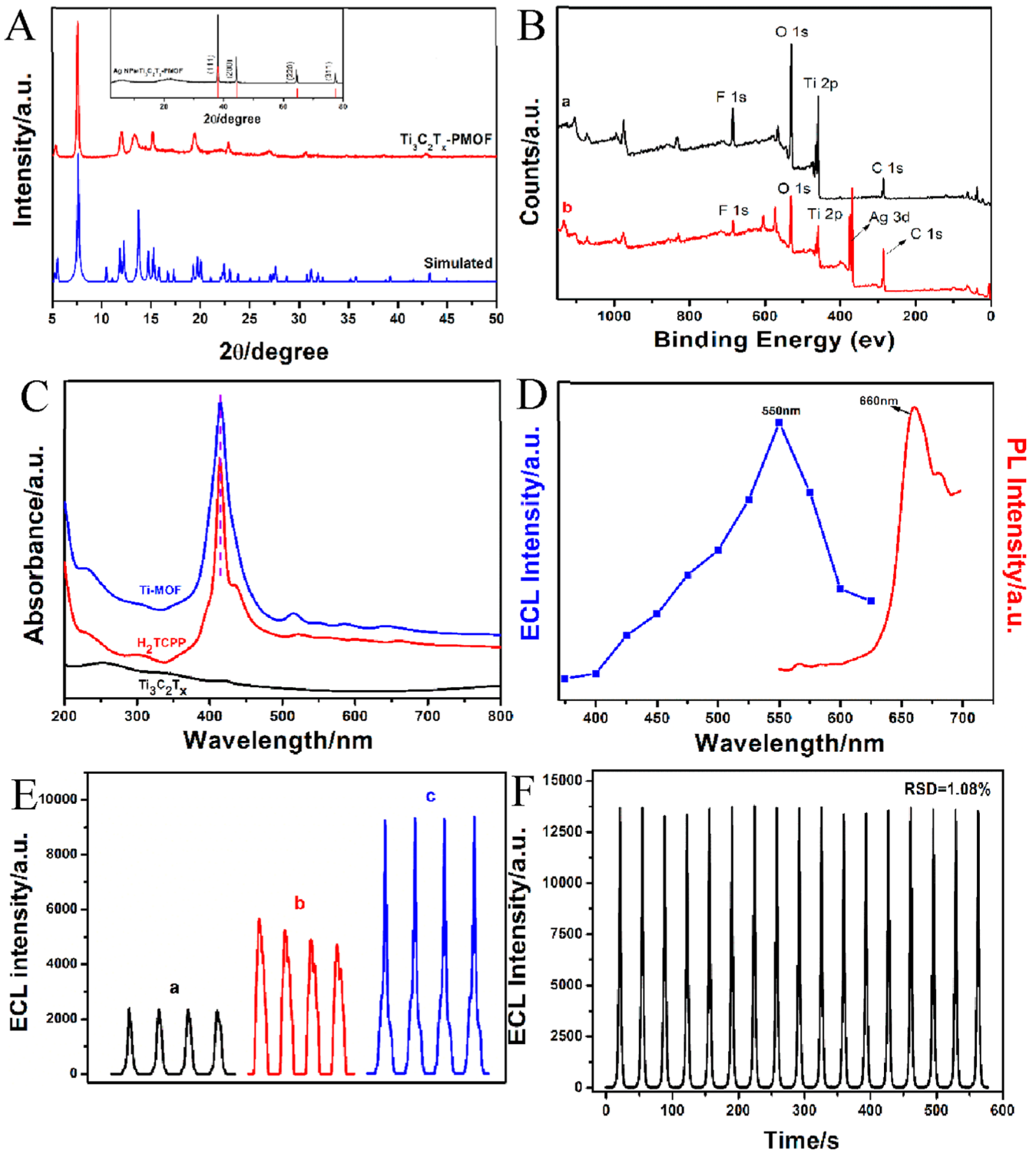

Figure 2. (A) XRD pattern of Ti3C2T$_x$-PMOF, the simulated, and Ag NPs/Ti3C2T$_x$-PMOF, (B) XPS spectra of Ti3C2T$_x$-PMOF (a) and Ag NPs/Ti3C2T$_x$-PMOF (b), (C) UV−vis absorption of Ti3C2T$_x$, H2TCPP and Ti3C2T$_x$-PMOF, (D) PL emission spectra and ECL spectra of Ti3C2T$_x$-PMOF, (E) ECL−time curves of H2TCPP (a), Ti3C2T$_x$-PMOF (b), and Ag NPs/Ti3C2T$_x$-PMOF (c), and (F) ECL emission from Ag NPs/Ti3C2T$_x$-PMOF under continuous cyclic scans.

particles only exist in the region of $Ti_3C_2T_x$-PMOF sheet, indicating that the composite materials have been successfully synthesized. As shown in TEM of Ag NPs (Figure S2), the size of Ag NPs was around 10 nm. From the high-resolution TEM (HRTEM) image (Figure 1E), the lattice fringe of Ag NPs was clearly observed. The XRD pattern of Ag NPs/$Ti_3C_2T_x$-PMOF is shown in the internal image of Figure 2A. It can be seen that the characteristic peaks of $Ti_3C_2T_x$-PMOF disappeared and the four diffraction peaks of Ag NPs appeared. The XPS spectra of $Ti_3C_2T_x$-PMOF and Ag NPs/$Ti_3C_2T_x$-PMOF are shown in Figure 2B. The difference between curve a and curve b in Figure 2B is the characteristic peak of Ag 3d. After composited

https://doi.org/10.1021/acsami.2c00497
ACS Appl. Mater. Interfaces 2022, 14, 23726−23733

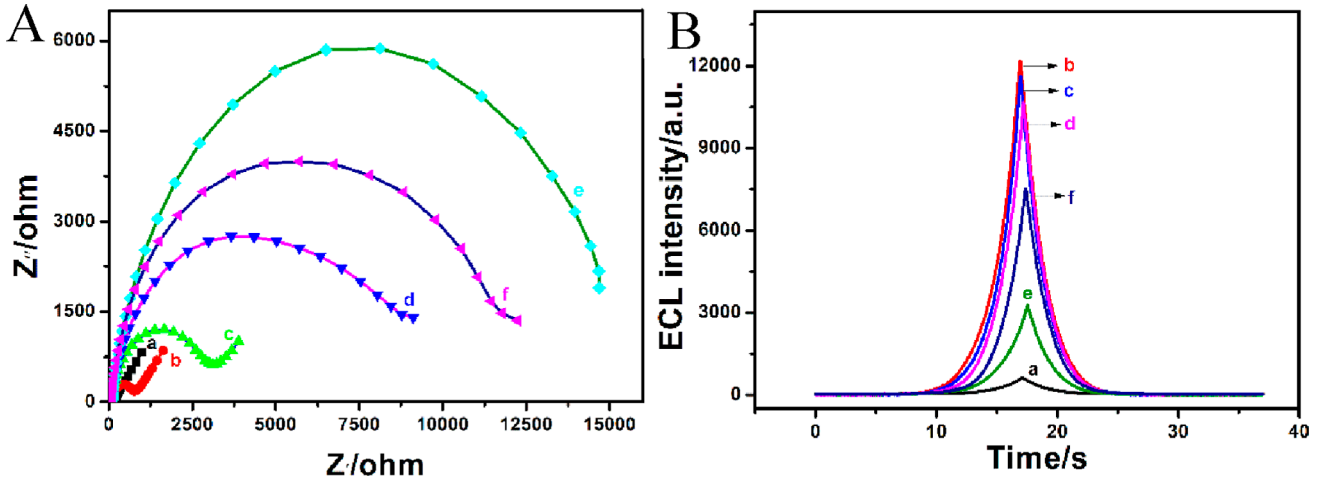

Figure 3. (A) EIS and (B) ECL responses of (a) bare GC electrode, (b) Ag NPs/Ti3C2T$_x$-PMOF/GCE, (c) C-DNA/Ag NPs/Ti3C2T$_x$-PMOF/GCE, (d) BSA/C-DNA/Ag NPs/Ti3C2T$_x$-PMOF/GCE, (e) Fc-DNA/BSA/C-DNA/Ag NPs/Ti3C2T$_x$-PMOF/GCE, and (f) s-DNA/Fc-DNA/BSA/C-DNA/Ag NPs/Ti3C2T$_x$-PMOF/GCE. The EIS curve was obtained in electrolyte containing 5 mM of $[Fe(CN)6]^{3-/4-}$ and 0.1 M KCl.

with Ag NPs, the characteristic peak of Ag 3d appeared in X-ray photoelectron spectroscopy (XPS) spectra of Ag NPs/$Ti_3C_2T_x$-PMOF. The results of XPS also indicate the successful synthesis of the composite. The high-resolution XPS spectra of Ag NPs/$Ti_3C_2T_x$-PMOF are shown in the Supporting Information. As shown in Figure S3A, the binding energies of Ti 2p for Ti−C, Ti−OH, Ti−O (2p3/2), Ti−F, and Ti−O (2p1/2) are 455.47, 456.55, 459.22, 462.91, and 465.05 eV, respectively, and the peak ranging from 454 to 457 eV suggests the presence of low-valence Ti species.[26,27] The three binding energy peaks of 530.64, 532.17, and 533.51 eV in O 1s spectra (Figure S3B) correspond to the surface of Ti−O, C═O, and C−O.[28,29] The C 1s spectrum (Figure S3C) can be divided into four peaks at 281.88, 284.76, 286.13, and 288.70 eV, which could correspond to the Ti−C, C−C, C−O, and C−F, respectively.[29] Additionally, Ag 3d (Figure S3D) exhibits two obvious peaks at 368.30 and 374.30 eV, which correspond to Ag $3d_{5/2}$ and Ag $3d_{3/2}$, respectively.[30] The difference between the two peaks is 6.0 eV, suggesting the presence of Ag (0).[30]

The optical properties of nanomaterials are also shown in Figure 2. As described in Figure 2C, H_2TCPP and $Ti_3C_2T_x$-PMOF show a high-energy Soret band and low Q bands. The Soret bands of H_2TCPP and $Ti_3C_2T_x$-PMOF were located at 415 nm, but the full widths at half-maxima (fwhm) were different. The broadening of absorption spectra of $Ti_3C_2T_x$-PMOF indicates the electronic interactions between porphyrin molecules owing to their heterogeneity.[31] The fluorescence spectrum and ECL emission spectrum of $Ti_3C_2T_x$-PMOF are shown in Figure 2D. The red-curve photoluminescence (PL) emission peak is located at 660 nm (the excitation wavelength at 416 nm), and the ECL maximum wavelength is located at 550 nm. The ECL behaviors of different modified electrodes in the same electrolyte (0.1 M, PBS containing 0.1 M $K_2S_2O_8$) are exhibited in Figure 2E. The ECL intensity of $Ti_3C_2T_x$-PMOF was two times higher than that of H_2TCPP. This phenomenon is caused by the immobilization of H_2TCPP organic linkers in the 2D MOF structure. The nanosheet structure of $Ti_3C_2T_x$-PMOF suppressed intramolecular free motions of H_2TCPP and nonradiative transitions, which makes it easy to obtain excited states via the ECL route.[32] After being modified with Ag NPs, the ECL intensity enhanced dramatically (curve c). This may be attributed to the co-reactant accelerator role of Ag NPs.[14,15] The ECL stability of Ag NPs/$Ti_3C_2T_x$-PMOF is shown in Figure 2F. After 17 consecutive cycles of scanning, the relative standard deviation of the peak is 1.08%.

Feasibility of the Biosensor. Each step of the GCE surface modification process was checked by electrochemical impedance spectroscopy (EIS) and ECL response, as shown in Figure 3. The semicircular region corresponded to the variations of electrode surface resistance and electron transfer kinetics in the redox process.[33] As depicted in Figure 3A, the bare GCE (curve a) has an almost linear curve, illustrating its great conductivity. The diameter of the semicircle (curve b) increased slightly after the Ag NPs/$Ti_3C_2T_x$-PMOF was modified on the GCE surface. The presence of Ag NPs/$Ti_3C_2T_x$-PMOF hinders the charge transfer between the solution and electrode surface. Due to the mutual exclusivity between negative charge of the DNA phosphate skeleton and the $[Fe(CN)_6]^{3-/4-}$, the diameter of the semicircle increased obviously after being modified with C-DNA (curve c) and Fc-DNA (curve e). After being incubated with S-DNA, part of the Fc-DNA was taken away from the GCE surface, and the diameter of the semicircle was decreased (curve f).

The ECL response for each modified GCE was also measured and is shown in Figure 3B. Corresponding with the EIS results, the ECL response of the bare GCE was so low to be neglected (curve a). After being modified with Ag NPs/$Ti_3C_2T_x$-PMOF, the GCE exhibited a strong ECL signal (curve b). Because of the weak electrical conductivity of biological macromolecules, the ECL signal of Ag NPs/$Ti_3C_2T_x$-PMOF was slightly reduced after being modified with the C-DNA (curve c) and BSA (curve d). Due to the energy resonance transfer between Ag NPs/$Ti_3C_2T_x$-PMOF and ferrocene, the ECL signal reduced markedly after the Fc-DNA was modified on the GCE (curve e). With the incubation of S-DNA, Fc-DNA was removed from the GCE, and the ECL signal was recovered obviously (curve f).

Optimization of Biosensor Measurement Conditions. In order to obtain the best performance of the bipedal 3D walker-based ECL biosensor, some measurement conditions were studied: the amount of A1 (A2), the concentration of W1 (W2), the incubation time of the bipedal 3D walker, the concentration of C-DNA, and the concentration of enzyme

https://doi.org/10.1021/acsami.2c00497
ACS Appl. Mater. Interfaces 2022, 14, 23726−23733

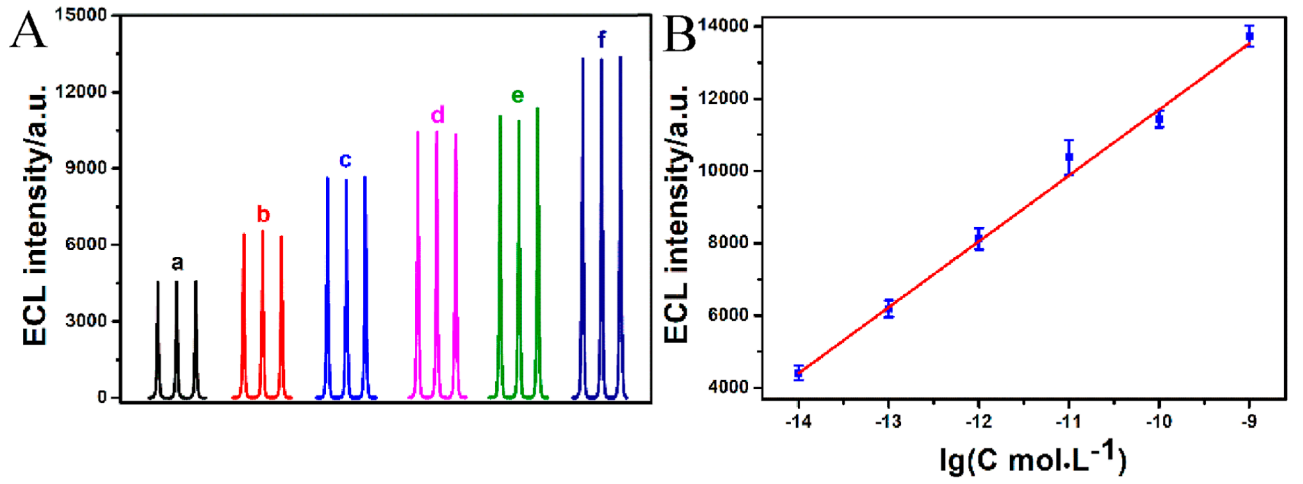

Figure 4. (A) ECL response for different ORAOV1 levels and (B) Corresponding calibration curves for the biosensor [(a) 10 fM, (b) 100 fM, (c) 1 pM, (d) 10 pM, (e) 100 pM, and (f) 1 nM].

(Nb.BbvCI). The amount of track strands anchored on per Fe_3O_4 was controlled by changing the volume of A1 (A2), and the concentration was fixed at 2 μM. As described in Figure S4A, the A1 volume corresponding to the peak of ECL intensity was 7.5 μL. The ECL intensity decreased slightly after the track strands exceeded 7.5 μL, which may be attributed to the steric hindrance. Hence, the optimal concentration was 7.5 μL. The concentration of W1 was an important parameter for this biosensor (Figure S4B). Hence, the W1 concentration effect was investigated in the range from 0.5 to 10 μM. With the increasing amount of W1, the ECL response increased until the concentration reached 5 μM. After the W1 concentration exceeded 5 μM, the ECL response decreased, which may be attributed to the steric hindrance between walkers and nicking endonuclease. Thus, the best concentration of W1 was 5 μM. As described in Figure S3C, a suitable walking time would improve the biosensor performance. With the increase of walking time, the ECL intensity of the biosensor was increased. When incubated for 2 h, the ECL intensity reached the highest, and it did not increase with the incubation time. Hence, the optimal walking time was 2 h. The concentration of C-DNA was optimized in the range of 2−10 μM (Figure S4D). After the concentration reached 6 μM, the ECL intensity changes tended to flatten. Hence, the best concentration was 6 μM. The optimization of conditions for enzyme concentration is shown in Figure S4E. The biosensor response signal of different enzyme concentrations was studied in the range of 0−12.5 U/mL. As shown in Figure S4E, the ECL response increases with the increase of enzyme concentration, and the ECL signal reaches the peak at an enzyme concentration of 10 U/mL.

Analytical Performance of the Biosensor. The ECL biosensor was challenged by different concentrations of ORAOV 1 under the optimal experimental conditions to verify the analytical performance of the biosensor. A high concentration of ORAOV 1 can release more S-DNA, and then, S-DNA will remove the Fc-DNA and recover the ECL response signal. Hence, the ECL response signal increased as the ORAOV 1 concentration increased. As described in Figure 4A, the ECL intensity increased with the increase of target concentration in the range of 10 fM−1 nM, and the ECL signal increased linearly with the logarithm target concentration increasing in the range of 10 fM−1 nM (Figure 4B). The corresponding linear equation is I = 1826.44 lg c + 29 967.76 (R^2 = 0.997), where I represents the ECL intensity and c represents the concentration of ORAOV 1. The limit detection for ORAOV 1 was 3.3 fM (S/N = 3). Compared with the previous reports (Table S2), this biosensor possesses lower LOD and wider detection range for ORAOV 1.

Selectivity and Stability of the Proposed Biosensor. The selectivity of this biosensor was evaluated by testing the response of different DNA molecules including blank sample, 10 pM single-base mismatch (sm-DNA), 10 pM double-base mismatch (dm-DNA), 10 pM three-base mismatch (tm-DNA), 1 pM ORAOV 1, and the mixture sample (containing 1 pM ORAOV 1, 10 pM sm-DNA, 10 pM dm-DNA, and 10 pM tm-DNA). As depicted in Figure 5, the ECL intensity of blank

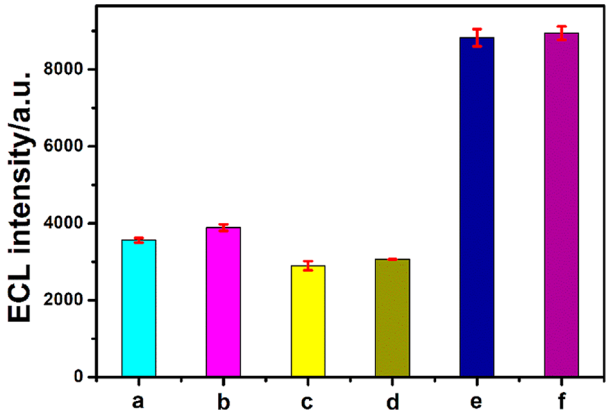

Figure 5. Selectivity of the ECL biosensor for different targets. These included (a) blank, (b) single-base mismatch, (c) double-base mismatch, (d) three-base mismatch, (e) 1 pM ORAOV 1, and (f) mixture (1 pM ORAOV 1 and 10 pM single-base mismatch, double-base mismatch, and three-base mismatch).

sample, sm-DNA, dm-DNA, and tm-DNA sample showed no obvious recovery, but the target and the mixture sample were recovered significantly. Therefore, the proposed biosensor has high specificity for ORAOV 1. The stability of the biosensor was tested by keeping the biosensor at 4 °C for1 week. As shown in Figure S5, the test found that the ECL intensity hardly changed (96.12% of the initial signal). Hence, the biosensor has great stability.

https://doi.org/10.1021/acsami.2c00497
ACS Appl. Mater. Interfaces 2022, 14, 23726−23733

Analytical Performance of the Biosensor in a Real Sample. The standard addition method was applied to measure the practical application of the biosensor. The saliva supernatant was collected from healthy volunteers and diluted 10 times by PBS (0.1 M, pH 7.4). Different concentrations of ORAOV 1 were spiked in the treated saliva and the recovery is shown in Table S3. The results indicated that the biosensor for detection of ORAOV 1 can be applied in clinical research.

CONCLUSIONS

In this work, $Ti_3C_2T_x$ MXene and H_2TCPP were respectively selected as the metal precursor and organic ligand to synthesize MOF for the first time. The ECL property of H_2TCPP was inherited and carried forward by the new MOF. After combining with Ag NPs, the ECL properties of $Ti_3C_2T_x$-PMOF were greatly improved. Then, a highly sensitive ECL biosensor for detection of ORVOA1 was constructed based on the Ag NPs/$Ti_3C_2T_x$-PMOF complex materials and the bipedal 3D walker amplified strategy. In the optimal conditions, the ECL biosensor exhibited a wider detection range of 10 fM−1 nM as well as a lower LOD of 3.3 fM. In addition, the biosensor also possesses the high stability and selectivity. Hence, Ag NPs/$Ti_3C_2T_x$-PMOF complex materials can be used as a potential material to build the ECL biosensor.

ASSOCIATED CONTENT

Supporting Information

The Supporting Information is available free of charge at https://pubs.acs.org/doi/10.1021/acsami.2c00497.

Chemical, materials, and apparatus (PDF)

AUTHOR INFORMATION

Corresponding Authors

Xing-Pei Liu − *Key Laboratory of Structure and Functional Regulation of Hybrid Materials (Ministry of Education), School of Chemistry and Chemical Engineering, Anhui University, Hefei, Anhui 230601, China*; Email: 414043594@qq.com

Chang-Jie Mao − *Key Laboratory of Structure and Functional Regulation of Hybrid Materials (Ministry of Education), School of Chemistry and Chemical Engineering, Anhui University, Hefei, Anhui 230601, China*; orcid.org/0000-0002-5563-4153; Email: maochangjie@sina.com

Authors

Yu-Ping Wei − *Key Laboratory of Structure and Functional Regulation of Hybrid Materials (Ministry of Education), School of Chemistry and Chemical Engineering, Anhui University, Hefei, Anhui 230601, China*

Jing-Shuai Chen − *Key Laboratory of Structure and Functional Regulation of Hybrid Materials (Ministry of Education), School of Chemistry and Chemical Engineering, Anhui University, Hefei, Anhui 230601, China*

Bao-Kang Jin − *Key Laboratory of Structure and Functional Regulation of Hybrid Materials (Ministry of Education), School of Chemistry and Chemical Engineering, Anhui University, Hefei, Anhui 230601, China*

Complete contact information is available at: https://pubs.acs.org/10.1021/acsami.2c00497

Notes

The authors declare no competing financial interest.

ACKNOWLEDGMENTS

This work was supported by the National Natural Science Foundation of China (21976001) and Open fund for Discipline Construction of the Institute of Physical Science and Information Technology.

REFERENCES

(1) Zhang, C. J.; Pinilla, S.; Mcevoy, N.; Cullen, C. P.; Anasori, B.; Long, E.; Park, S.-H.; Seral-Ascaso, A.; Shmeliov, A.; Krishnan, D.; Morant, C.; Liu, X.; Duesberg, G. S.; Gogotsi, Y.; Nicolosi, V. Oxidation stability of colloidal two-dimensional titanium carbides (MXenes). *Chem. Mater.* **2017**, *29*, 4848−4856.

(2) Zhang, J.; Zhao, Y.; Guo, X.; Chen, C.; Dong, C.-L.; Liu, R.-S.; Han, C.-P.; Li, Y.; Gogotsi, Y.; Wang, G. Single platinum atoms immobilized on an MXene as an efficient catalyst for the hydrogen evolution reaction. *Nat. Catal.* **2018**, *1*, 985−992.

(3) Hart, J. L.; Hantanasirisakul, K.; Lang, A. C.; Anasori, B.; Pinto, D.; Pivak, Y.; van Omme, J. T.; May, S. J.; Gogotsi, Y.; Taheri, M. L. Control of MXenes' electronic properties through termination and intercalation. *Nat. Commun.* **2019**, *10*, 522.

(4) Qin, L.; Jiang, J.; Tao, Q.; Wang, C.; Person, I.; Fahlman, M.; Persson, P. O.; Hou, L.; Rosen, J.; Zhang, F. A flexible semi-transparent photovoltaic supercapacitor based on water-processed MXene electrodes. *J. Mater. Chem. A* **2020**, *8*, 5467−5475.

(5) Zhang, J.; Kerr, E.; Usman, K. A. S.; Doeven, E. H.; Francis, P. S.; Henderson, L. C.; Razal, J. M. Cathodic electrogenerated chemiluminescence of tris(2,2′-bipyridine)ruthenium(ii) and peroxydisulfate at pure Ti3C2Tx MXene electrodes. *Chem. Commun.* **2020**, *56*, 10022−10025.

(6) Zhang, H.; Wang, Z. H.; Zhang, Q. X.; Wang, F.; Liu, Y. Ti3C2 MXenes nanosheets catalyzed highly efficient electrogenerated chemiluminescence biosensor for the detection of exosomes. *Biosens. Bioelectron.* **2019**, *124*−*125*, 184−190.

(7) Wu, H.; Almalki, M.; Xu, X.; Lei, Y.; Ming, F.; Mallick, A.; Roddatis, V.; Lopatin, S.; Shekhah, O.; Eddaoudi, M.; Alshareef, H. N. MXene derived metal-organic frameworks. *J. Am. Chem. Soc.* **2019**, *141*, 20037−20042.

(8) Han, Q.; Wang, C.; Li, Z.; Wu, J.; Liu, P. K.; Mo, F.; Fu, Y. Multifunctional zinc oxide promotes electrochemiluminescence of porphyrin aggregates for ultrasensitive detection of copper ion. *Anal. Chem.* **2020**, *92*, 3324−3331.

(9) Gan, X.; Han, D.; Wang, J.; Liu, P.; Li, X.; Zheng, Q.; Yan, Y. A highly sensitive electrochemiluminescence immunosensor for h-FABP determination based on self-enhanced luminophore coupled with ultrathin 2D nickel metal-organic framework nanosheets. *Biosens. Bioelectron.* **2021**, *171*, 112735.

(10) Wei, Y.-P.; Zhang, Y. W.; Chen, J. S.; Mao, C. J.; Jin, B. K. An electrochemiluminescence biosensor for p53 antibody based on Zn-MOF/GO nanocomposite and Ag+-DNA amplification. *Microchim. Acta* **2020**, *187*, 455.

(11) Cai, W.-R.; Zeng, H.-B.; Xue, H.-G.; Marks, R. S.; Cosnier, S.; Zhang, X.-J.; Shan, D. Enhanced electrochemiluminescence of porphyrin-based metal-organic frameworks controlled via coordination modulation. *Anal. Chem.* **2020**, *92*, 1916−1924.

(12) Jiang, Y.; Zhang, X.; Pei, L.; Yue, S.; Ma, L.; Zhou, L.; Huang, Z.; He, Y.; Gao, J. Silver nanoparticles modified two-dimensional transition metal carbides as nanocarriers to fabricate acetycholinesterase-based electrochemical biosensor. *Chem. Eng. J.* **2018**, *339*, 547−556.

(13) Zou, G.; Zhang, Z.; Guo, J.; Liu, B.; Zhang, Q.; Fernandez, C.; Peng, Q. Synthesis of MXene/Ag composites for extraordinary long cycle lifetime lithium storage at high rates. *ACS Appl. Mater. Interfaces* **2016**, *8*, 22280−22286.

(14) Du, X.; Jiang, D.; Liu, Q.; Qian, J.; Mao, H.; Wang, K. Enhanced electrochemiluminescence sensing platform using nitrogen-doped graphene as a novel two-dimensional mat of silver nanoparticles. *Talanta* **2015**, *132*, 146−149.

(15) Jiang, M.-H.; Lu, P.; Lei, Y.-M.; Chai, Y.-Q.; Yuan, R.; Zhuo, Y. Self-accelerated electrochemiluminescence emitters of Ag@SnO2 nanoflowers for sensitive detection of cardiac troponin T. *Electrochim. Acta* **2018**, *271*, 464−471.
(16) Jiang, L.; Zeng, X.; Wang, Z.; Ji, N.; Zhou, Y.; Liu, X.; Chen, Q. Oral cancer overexpressed 1 (ORAOV1) regulates cell cycle and apoptosis in cervical cancer HeLa cells. *Mol. Cancer* **2010**, *9*, 20.
(17) Zhai, C.; Li, Y.; Mascarenhas, C.; Lin, Q.; Li, K.; Vyrides, I.; Grant, C. M.; Panaretou, B. The function of ORAOV1/LTO1, a gene that is overexpressed frequently in cancer: essential roles in the function and biogenesis of the ribosome. *Oncogene* **2014**, *33*, 484−494.
(18) Zhang, L.; Liu, X.; Xu, X.; Zhang, N.; Jiang, W.; Jiang, W. A bipedal-unequivalent three-dimensional DNA walker and its biosensing application. *Sens. Actuators, B* **2021**, *327*, 128942.
(19) Lv, H.; Chen, A.; Cheng, W.; Kong, L.; Zhao, M.; Ding, S.; Ju, H.; Cheng, W. Efficient DNA walker guided with well-regulated interfacial tracks for ultrasensitive electrochemiluminescence biosensing. *Anal. Chem.* **2020**, *92*, 15624−15631.
(20) Yang, F.; Yang, F.; Tu, T.-T.; Liao, N.; Chai, Y.-Q.; Yuan, R.; Zhuo, Y. A synergistic promotion strategy remarkably accelerated electrochemiluminescence of SnO2 QDs for MicroRNA detection using 3D DNA walker amplification. *Biosens. Bioelectron.* **2021**, *173*, 112820.
(21) Qi, Y.; Zhai, Y.; Fan, W.; Ren, W.; Li, Z.; Liu, C. Click chemistry-actuated digital DNA walker confined on a single particle toward absolute microRNA quantification. *Anal. Chem.* **2021**, *93*, 1620.
(22) Li, C.; Li, H.; Ge, J.; Jie, G. Versatile fluorescence detection of microRNA based on novel DNA hydrogel-amplified signal probes coupled with DNA walker amplification. *Chem. Commun.* **2019**, *55*, 3919.
(23) Zhu, M.; Zhong, X.; Deng, H.; Huang, L.; Yuan, R.; Yuan, Y. Dependent signal quenching and enhancing triggered by bipedal DNA walker for ultrasensitive photoelectrochemical biosensor. *Biosens. Bioelectron.* **2019**, *143*, 111618.
(24) VahidMohammadi, A.; Mojtabavi, M.; Caffrey, N. M.; Wanunu, M.; Beidaghi, M. Assembling 2D MXenes into highly stable pseudocapacitive electrodes with high power and energy densities. *Adv. Mater.* **2019**, *31*, 1806931.
(25) Amstad, E.; Textor, M.; Reimhult, E. Stabilization and functionalization of iron oxide nanoparticles for biomedical applications. *Nanoscale* **2011**, *3*, 2819−2843.
(26) Chang, P.; Kuai, Z. Y.; Li, X. Z.; Lian, S. S.; Jiang, D. L.; Tang, J. F.; Li, L.; Wu, R. X.; Wu, A. J.; Chen, S. Facile synthesis of Ag nanoparticles/$Ti_3C_2T_x$/polyacrylamide composite hydrogel as efficient catalyst for methylene blue and 4-nitrophenol reduction. *Mater. Des.* **2021**, *210*, 110061.
(27) Zou, G.; Zhang, Z.; Guo, J.; Liu, B.; Zhang, Q.; Fernandez, C.; Peng, Q. Synthesis of mxene/ag composites for extraordinary long cycle lifetime lithium storage at high rates. *ACS Appl. Mater. Interfaces* **2016**, *8*, 22280−22286.
(28) Wang, Y.; Zeng, Z.; Qiao, J.; Dong, S.; Liang, Q.; Shao, S. Ultrasensitive determination of nitrite based on electrochemical platform of AuNPs deposited on PDDA-modified MXene nanosheets. *Talanta* **2021**, *221*, 121605.
(29) Wojciechowski, T.; Rozmysłowska-Wojciechowska, A.; Matyszczak, G.; Wrzecionek, M.; et al. Ti2C MXene modified with ceramic oxide and noble metal nanoparticles: synthesis, morphostructural properties, and high photocatalytic activity. *Inorg. Chem.* **2019**, *58*, 7602−7614.
(30) Jiang, Y.; Zhang, X.; Pei, L.; Yue, S.; Ma, L.; Zhou, L.; Huang, Z.; He, Y.; Gao, J. Silver nanoparticles modified two-dimensional transition metal carbides as nanocarriers to fabricate acetycholinesterase-based electrochemical biosensor. *Chem. Eng. J.* **2018**, *339*, 547−556.
(31) Mandal, S.; Nayak, S. K.; Mallampalli, S.; Patra, A. Surfactant-assisted porphyrin based hierarchical nano/micro assemblies and their efficient photocatalytic behavior. *ACS Appl. Mater. Interfaces* **2014**, *6*, 130−136.
(32) Han, Q.; Wang, C.; Liu, P.; Zhang, G.; Song, L.; Fu, Y. Achieving synergistically enhanced dual-mode electrochemiluminescent and electrochemical drug sensors via a multi-effect porphyrin-based metal-organic framework. *Sens. Actuators, B* **2021**, *330*, 129388.
(33) Fan, Z.; Yao, B.; Ding, Y.; Zhao, J.; Xie, M.; Zhang, K. Entropy-driven amplified electrochemiluminescence biosensor for RdRp gene of SARS-CoV-2 detection with self-assembled DNA tetrahedron scaffolds. *Biosens. Bioelectron.* **2021**, *178*, 113015.

https://doi.org/10.1021/acsami.2c00497
ACS Appl. Mater. Interfaces 2022, 14, 23726−23733